Electrostatically confined trilayer graphene quantum dots

M. Mirzakhani,[1,2,*] M. Zarenia,[1,†] P. Vasilopoulos,[3,‡] and F. M. Peeters[1,§]
[1]*Department of Physics, University of Antwerp, Groenenborgerlaan 171, B-2020 Antwerp, Belgium*
[2]*School of Physics, Damghan University, P. O. Box: 36716-41167, Damghan, Iran*
[3]*Department of Physics, Concordia University, 7141 Sherbrooke West, Montreal, Quebec, Canada H4B 1R6*
(Received 23 December 2016; revised manuscript received 16 March 2017; published 21 April 2017)

Electrically gating of trilayer graphene (TLG) opens a band gap offering the possibility to electrically engineer TLG quantum dots. We study the energy levels of such quantum dots and investigate their dependence on a perpendicular magnetic field B and different types of stacking of the graphene layers. The dots are modeled as circular and confined by a truncated parabolic potential which can be realized by nanostructured gates or position-dependent doping. The energy spectra exhibit the intervalley symmetry $E^e_K(m) = -E^h_{K'}(m)$ for the electron (e) and hole (h) states, where m is the angular momentum quantum number and K and K' label the two valleys. The electron and hole spectra for $B = 0$ are twofold degenerate due to the intervalley symmetry $E_K(m) = E_{K'}[-(m+1)]$. For both ABC [$\alpha = 1.5$ (1.2) for large (small) R] and ABA ($\alpha = 1$) stackings, the lowest-energy levels show approximately a $R^{-\alpha}$ dependence on the dot radius R in contrast with the $1/R^3$ one for ABC-stacked dots with infinite-mass boundary. As functions of the field B, the oscillator strengths for dipole-allowed transitions differ drastically for the two types of stackings.

DOI: 10.1103/PhysRevB.95.155434

I. INTRODUCTION

Due to the absence of a gap in monolayer graphene (MLG), the charge carriers can tunnel through arbitrarily high and wide potential barriers at normal incidence, an effect known as Klein tunneling [1]. However, it is possible to realize quasibound states [2] with such potential barriers that become more localized with increasing magnetic field [3]. Also, a spatially modulated gap [4] can localize electrons in graphene.

Although theoretical works predict that monolayer graphene on a hexagonal boron nitride (h-BN) substrate [5,6] may exhibit a large enough gap, about 50 meV wide, to confine carriers through a gate-defined quantum dot (QD) in the absence of a magnetic field, this is expected to be extremely challenging experimentally. Furthermore, uncontrolled weakly localized states are created by the substrate-induced disorder potential in graphene on SiO_2 [7,8] and in suspended graphene nanoribbons [9]. Imperfect confinement can be realized by p-n junctions [10]. However, the application of a magnetic field can suppress Klein tunneling, leading to bound states. Controlled confinement by a combination of magnetic and electrostatic fields has been investigated both theoretically [3,11,12] and experimentally [13,14]. Graphene QDs can be fabricated by direct etching of graphene sheets in which the edges have a strong influence on their electronic properties [15–19].

In contrast to MLG, an external gate potential or position-dependent doping can induce a tunable band gap in the energy spectrum of bilayer graphene (BLG) [20]. This makes it possible to realize electrostatically defined BLG QDs. Moreover, in this type of QDs the precise shape of the edges is no longer important because confinement can be realized far away from the edges of the BLG sheet. Such QDs have been studied theoretically in Refs. [21,22] and experimentally realized by two different groups [23,24].

It is also known that the weak van der Waals interlayer coupling in graphene multilayers exerts a significant influence on the electronic band structure offering various types of quasiparticles in the low-energy electronic spectrum [25,26]. Therefore, now that QDs have been experimentally realized in BLG [23,24], it is of interest to study also QDs with three or more layers and with different types of stacking arrangements, e.g., ABC or ABA, and assess the differences in properties from BLG. Experimental realization of few-layer graphene is within the grasp of current technology since few-layer graphene sheets can be fabricated with large areas by mechanical exfoliation [27,28] and by chemical techniques [29–31] from graphite with controlled stacking order. References [32–34] are examples of experimental studies of electronic and transport properties in TLG. Similar to BLG, applying an electric gate induces a band gap in the energy spectrum of TLG [32,34–37]. The difference in the stacking order of layers in extended graphene was shown to strongly affect the electric-field-induced band gap in Ref. [38] with the one of the ABC stacking being much larger than that of the ABA one.

The aim of this study is to focus on the energy levels of electrostatically defined QDs on trilayer graphene (TLG), in the presence or absence of a magnetic field, and contrast the results for ABC and ABA stackings. In doing so, we extend significantly the results of our recent work [39], in which only the ABC stacking was studied and the dot confinement resulted from an infinite-mass boundary condition. We consider, here, parabolic confinement by means of external gates or a position-dependent doping, which eliminates the effects due to the edges.

The paper is organized as follows. In Sec. II, we present the basics of the model of a QD in TLG for ABC and ABA stackings. In Sec. III, we present numerical results for the two stackings and the corresponding oscillator strengths. A summary and concluding remarks follow in Sec. IV.

*mohammad.mirzakhani@uantwerpen.be
†mohammad.zarenia@uantwerpen.be
‡p.vasilopoulos@concordia.ca
§francois.peeters@uantwerpen.be

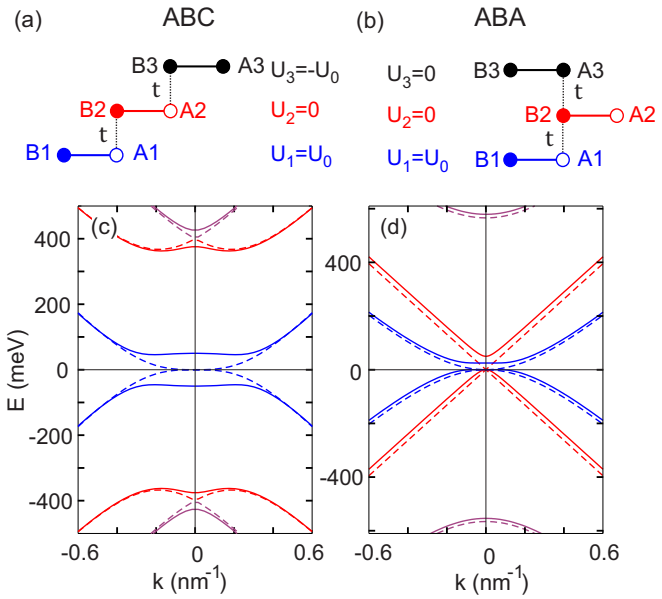

FIG. 1. (Upper panels) Schematics of interlayer couplings in TLG for (a) ABC stacking and (b) ABA stacking. A_i and B_i, $i = 1,2,3$, are the layer sublattices, $t \approx 400$ meV the interlayer coupling, and U_i ($i = 1,2,3$) the potentials applied to the layers. (Lower panels) Low-energy band structures of (c) ABC- and (d) ABA-stacked TLG in the absence of bias ($U_i = 0$, dashed curves) or in the presence of bias (solid curves) as specified in the upper panels with $U_0 = 50$ meV.

II. MODEL

We consider TLG as three honeycomb sheets, of cova-lent-bonded carbon atoms, stacked in an ABC or ABA manner; both stacking configurations are realized experimentally [27–31]. The upper panels in Fig. 1 show schematically these stackings and the potentials U_i applied to the layers. We assume that hopping between planes takes place only between atoms which are on top of each other in neighboring layers. Thus, the whole model is defined by the parameters v_F and t.

A. ABC stacking

The Hamiltonian describing a Dirac electron in the presence of a circular barrier in ABC-stacked TLG is given by [40,41]

$$\mathcal{H} = \begin{pmatrix} U_1 & v_F\pi & t & 0 & 0 & 0 \\ v_F\pi^\dagger & U_1 & 0 & 0 & 0 & 0 \\ t & 0 & U_2 & v_F\pi^\dagger & 0 & 0 \\ 0 & 0 & v_F\pi & U_2 & 0 & t \\ 0 & 0 & 0 & 0 & U_3 & v_F\pi \\ 0 & 0 & 0 & t & v_F\pi^\dagger & U_3 \end{pmatrix}, \quad (1)$$

where U_i ($i = 1,2,3$) are the potentials applied to the graphene layers and $v_F = 3a\gamma_0/2\hbar \approx 10^6$ m/s is the Fermi velocity of monolayer graphene, the intralayer nearest-neighbor hopping is $\gamma_0 \approx 3$ eV, and the carbon-carbon distance $a \approx 1.42$ Å [42]. $\pi = \pi_x + i\tau\pi_y$ and $\pi^\dagger = \pi_x - i\tau\pi_y$ are the momentum operators, in the presence of a magnetic field B perpendicular to the layers, given by $\boldsymbol{\pi} = -i\hbar\boldsymbol{\nabla} + e\mathbf{A}$. The values $\tau = +1$ and -1 distinguish the K and K' valleys, respectively, and the vector potential $\mathbf{A}$, taken in the symmetric gauge, is $\mathbf{A}(\mathbf{r}) = (0, Br/2, 0)$. Here, we include only the nearest-neighbor interlayer coupling term $t \approx 400$ meV in Eq. (1), and do not take into account the hopping terms $\gamma_2, \ldots, \gamma_6$ [41], which are relevant to a description of finer details of the band structure such as the trigonal warping. The zero-field bulk band structure is shown in Fig. 1(c) for unbiased ($U_i = 0$, dashed curves) and biased (solid curves) ABC-stacked TLG as specified in Fig. 1(a) with $U_0 = 50$ meV. Comparing the continuum and tight-binding band structure [43] shows that the former one can be valid, approximately, in the energy range of -800 meV $\lessapprox E \lessapprox 800$ meV.

In polar coordinates r and θ, π and $\pi^\dagger$ take the form in dimensionless units

$$v_F\pi = -i\hbar v_F e^{i\tau\theta}\,[\partial/\partial\rho + (i\tau/\rho)\partial/\partial\theta - \tau\beta], \quad (2)$$

$$v_F\pi^\dagger = -i\hbar v_F e^{-i\tau\theta}\,[\partial/\partial\rho - (i\tau/\rho)\partial/\partial\theta + \tau\beta], \quad (3)$$

where $\rho = r/R$, $\beta = eBR^2/2\hbar = R^2/2l_B^2$, and $l_B = \sqrt{\hbar/eB}$ is the magnetic length.

Similar to Ref. [21], the eigenstate of the Hamiltonian (1) for the K valley is given by the six-component wave function $\Psi_{\rm ABC}$ and that for the K' valley by $\Psi'_{\rm ABC}$:

$$\Psi_{\rm ABC} = \begin{pmatrix} e^{im\theta}\phi_{A1} \\ ie^{i(m-1)\theta}\phi_{B1} \\ e^{im\theta}\phi_{B2} \\ ie^{i(m+1)\theta}\phi_{A2} \\ e^{i(m+2)\theta}\phi_{A3} \\ ie^{i(m+1)\theta}\phi_{B3} \end{pmatrix}, \ \Psi'_{\rm ABC} = \begin{pmatrix} e^{i(m+1)\theta}\phi_{A1} \\ ie^{i(m+2)\theta}\phi_{B1} \\ e^{i(m+1)\theta}\phi_{B2} \\ ie^{im\theta}\phi_{A2} \\ e^{i(m-1)\theta}\phi_{A3} \\ ie^{im\theta}\phi_{B3} \end{pmatrix}, \quad (4)$$

where $m = 0, \pm 1, \pm 2, \ldots$ is the angular momentum label and $\phi_{A1}, \ldots, \phi_{B3}$ are the envelope functions corresponding to different sublattices $A1, \ldots, B3$, respectively. For simplicity we removed the ρ dependence of all ϕ, i.e., we set $\phi_{A1} \equiv \phi_{A1}(\rho)$, etc. We note that the orbital angular momentum $\mathbf{L}_z = -i\hbar\partial_\theta$ does not commute with the Hamiltonian (1) and is not a conserved quantity. However, the wave functions (4) are eigenstates of the operator

$$\mathbf{J}_z^{\rm ABC} = \mathbf{L}_z + \frac{\hbar}{2}\begin{pmatrix} \alpha_1\mathbf{I} & 0 & 0 \\ 0 & -\mathbf{I} & 0 \\ 0 & 0 & \alpha_2\mathbf{I} \end{pmatrix} \pm \frac{\hbar}{2}\begin{pmatrix} -\boldsymbol{\sigma}_z & 0 & 0 \\ 0 & +\boldsymbol{\sigma}_z & 0 \\ 0 & 0 & -\boldsymbol{\sigma}_z \end{pmatrix}, \quad (5)$$

with eigenvalue m. $\mathbf{I}$ is the 2×2 identity matrix and $\boldsymbol{\sigma}_z$ the Pauli matrix. Further, $\{\alpha_1,\alpha_2\} \equiv \{1, -3\}$ ($\{-3,1\}$) and $+$ ($-$) refers to the K (K') valley.

The radial dependence of the wave-function components is described, in dimensionless units, by the coupled differential equations

$$\left[\frac{\partial}{\partial\rho} - \tau\frac{m-1}{\rho} - \tau\beta\rho\right]\phi_{B1} = (\varepsilon - u_1)\phi_{A1} - t'\phi_{B2},$$

$$\left[\frac{\partial}{\partial\rho} + \tau\frac{m}{\rho} + \tau\beta\rho\right]\phi_{A1} = -(\varepsilon - u_1)\phi_{B1},$$

$$\left[\frac{\partial}{\partial\rho}+\tau\frac{m+1}{\rho}+\tau\beta\rho\right]\phi_{A2}=(\varepsilon-u_2)\phi_{B2}-t'\phi_{A1},$$
$$\left[\frac{\partial}{\partial\rho}-\tau\frac{m}{\rho}-\tau\beta\rho\right]\phi_{B2}=-(\varepsilon-u_2)\phi_{A2}+t'\phi_{B3},$$
$$\left[\frac{\partial}{\partial\rho}-\tau\frac{m+1}{\rho}-\tau\beta\rho\right]\phi_{B3}=(\varepsilon-u_3)\phi_{A3},$$
$$\left[\frac{\partial}{\partial\rho}+\tau\frac{m+2}{\rho}+\tau\beta\rho\right]\phi_{A3}=-(\varepsilon-u_3)\phi_{B3}+t'\phi_{A2}, \quad (6)$$

where $E_0=\hbar v_F/R$, $\varepsilon=E/E_0$, $t'=t/E_0$, and $u_i=U_i/E_0$, $i=1,2,3$.

Now, we consider a circular-symmetric, position-dependent potential, such as the one described in Refs. [21,22]. In this case, we set $U_2=0$ and $U_1=-U_3=U_b(r)$, where $U_b(r)$ is taken to be the parabolic potential

$$U_b(r)=\begin{cases}U_0\,r^2/R^2, & r<R\\ U_0, & r>R\end{cases} \quad (7)$$

with U_0 the depth of the well. The position-dependent gap, which vanishes at the center of the QD, confines the carriers in the central region. This type of potential profile may be achieved by controlled doping of the surface or by applying gate electrodes [35,37,44,45].

B. ABA stacking

Using a simple model for ABC-stacked TLG, i.e., including only γ_0 and t, describing the nearest-neighbor intralayer and interlayer hopping, respectively, the ABA-stacked TLG [Fig. 1(b)] Hamiltonian reads as [40,46]

$$\mathcal{H}=\begin{pmatrix}U_1 & v_F\pi & t & 0 & 0 & 0\\ v_F\pi^\dagger & U_1 & 0 & 0 & 0 & 0\\ t & 0 & U_2 & v_F\pi^\dagger & t & 0\\ 0 & 0 & v_F\pi & U_2 & 0 & 0\\ 0 & 0 & t & 0 & U_3 & v_F\pi\\ 0 & 0 & 0 & 0 & v_F\pi^\dagger & U_3\end{pmatrix}, \quad (8)$$

where the corresponding wave functions $\Psi_{\rm ABA}$ (K valley) and $\Psi'_{\rm ABA}$ (K' valley) are

$$\Psi_{\rm ABA}=\begin{pmatrix}e^{im\theta}\phi_{A1}\\ ie^{i(m-1)\theta}\phi_{B1}\\ e^{im\theta}\phi_{B2}\\ ie^{i(m+1)\theta}\phi_{A2}\\ e^{im\theta}\phi_{A3}\\ ie^{i(m-1)\theta}\phi_{B3}\end{pmatrix},\ \Psi'_{\rm ABA}=\begin{pmatrix}e^{i(m-1)\theta}\phi_{A1}\\ ie^{im\theta}\phi_{B1}\\ e^{i(m-1)\theta}\phi_{B2}\\ ie^{i(m-2)\theta}\phi_{A2}\\ e^{i(m-1)\theta}\phi_{A3}\\ ie^{im\theta}\phi_{B3}\end{pmatrix}. \quad (9)$$

The wave functions (9) are eigenstates of the operator

$$\mathbf{J}_z^{\rm ABA}=\mathbf{L}_z\pm\frac{\hbar}{2}\begin{pmatrix}\mathbf{I} & 0 & 0\\ 0 & -\mathbf{I} & 0\\ 0 & 0 & \mathbf{I}\end{pmatrix}\pm\frac{\hbar}{2}\begin{pmatrix}-\boldsymbol{\sigma}_z & 0 & 0\\ 0 & +\boldsymbol{\sigma}_z & 0\\ 0 & 0 & -\boldsymbol{\sigma}_z\end{pmatrix}, \quad (10)$$

with eigenvalues m and $m-1$ at the K and K' valleys, respectively. Again $+$ $(-)$ refers to the K (K') valley.

The radial dependence of the wave function components are obtained from the coupled differential equations

$$\left[\frac{\partial}{\partial\rho}-\tau\frac{m-1}{\rho}-\tau\beta\rho\right]\phi_{B1}=(\varepsilon-u_1)\phi_{A1}-t'\phi_{B2},$$
$$\left[\frac{\partial}{\partial\rho}+\tau\frac{m}{\rho}+\tau\beta\rho\right]\phi_{A1}=-(\varepsilon-u_1)\phi_{B1},$$
$$\left[\frac{\partial}{\partial\rho}+\tau\frac{m+1}{\rho}+\tau\beta\rho\right]\phi_{A2}=(\varepsilon-u_2)\phi_{B2}-t'\phi_{A1}-t'\phi_{A3},$$
$$\left[\frac{\partial}{\partial\rho}-\tau\frac{m}{\rho}-\tau\beta\rho\right]\phi_{B2}=-(\varepsilon-u_2)\phi_{A2},$$
$$\left[\frac{\partial}{\partial\rho}-\tau\frac{m-1}{\rho}-\tau\beta\rho\right]\phi_{B3}=(\varepsilon-u_3)\phi_{A3}-t'\phi_{B2},$$
$$\left[\frac{\partial}{\partial\rho}+\tau\frac{m}{\rho}+\tau\beta\rho\right]\phi_{A3}=-(\varepsilon-u_3)\phi_{B3}. \quad (11)$$

By applying the potentials $U_1=U_0=50$ meV and $U_2=U_3=0$ [cf. Fig. 1(b)], one can induce an *asymmetric* band gap $\sim U_0/2$ [see Fig. 1(d)] in contrast with that for an ABC stacking, shown in Fig. 1(c), which is *symmetric* and equal to $2U_0$. For the position-dependent parabolic potential (7), one can solve Eqs. (6) and (11) numerically to obtain the energy levels. We use the standard finite-element package COMSOL MULTIPHYSICS [47] to obtain the eigenvalues and eigenfunctions of the systems of coupled Eqs. (6) and (11).

The COMSOL MULTIPHYSICS package finds the eigenvalues and corresponding eigenfunctions of a set of coupled partial differential equations. It employs the finite-element approach to solve the equations and allows us to check the numerical error at each iteration. The convergence criterion in our calculations is set to 10^{-16} ($=10^{-6}$ % relative error/tolerance) and it takes few iterations to reach convergence. For the boundary conditions, all the wave-function components are set to zero at infinity ($r\to\infty$) and no specific conditions are imposed at the origin so that the envelope functions can have finite values at the origin ($r=0$). At $r=R$ all envelope functions are required to be continuous. The size of the discrete mesh is also important and we decrease it until the results remain unchanged. We found that setting $r_\infty>20R$, as the computational box size, is sufficient for the results to remain unchanged. The confined (or bound) states are those where the corresponding spinors decay at large radial distance ($r\to\infty$) regardless of their energy, while the wave spinors of unconfined (or unbound) states are like plane waves which do not decay as r increases.

C. Oscillator strength

For electric dipole transitions between states m' and m, the oscillator strength is given by $|\langle\Psi_{m'}|re^{i\phi}|\Psi_m\rangle|^2$ [48] and can be expressed as

$$T=(T_{A1}+T_{B1}+T_{A2}+T_{B2}+T_{A3}+T_{B3})^2, \quad (12)$$

with

$$T_\nu=2\pi N'N\delta_{m',m+1}\int\phi_\nu^{m'}(\rho)\rho^2\phi_\nu^m(\rho)d\rho; \quad (13)$$

here, $\nu = A1, \ldots, B3$ and $N'(N)$ is the normalization constant for the states $m'(m)$. It is worth noting that we limit ourselves to intravalley transitions, and that the intervalley ones are absent. In the next section, we will evaluate the oscillator strength for both types of layer stacking.

III. NUMERICAL RESULTS

A. ABC stacking

Figures 2(a) and 2(b) show the energy spectrum as a function of the dot radius R, at the K (solid curves) and K' (dashed curves) valleys, with well depth $U_0 = 50$ meV, for (a) $B = 0$ T and (b) $B = 10$ T. These results are for the angular momentum values $m = -1$ (blue), $m = 0$ (green), and $m = 1$ (red). The spectrum consists of a series of discrete levels indicating the existence of confined states.

For zero magnetic field [Fig. 2(a)], the energy levels are separated by a gap, depending on the angular momentum and dot radius, which closes when R increases. Notice that bound states appear in the band gap $\sim 2U_0$. For $B = 0$, the energy levels are twofold degenerate due to the valley symmetry $E_K(m) = E_{K'}[-(m+1)]$ states. Furthermore, the energy levels in Fig. 2(a) exhibit the symmetry $E^e_K(m) = -E^h_{K'}(m)$ between the electron and hole states. However, in contrast to conventional two-dimensional (2D) semiconductor QDs [49], the $E^e(m) = E^e(-m)$ symmetry is broken for each valley. This is due to the breaking of the inversion symmetry in the presence of an induced perpendicular electric field in gated TLG QDs. For $B \neq 0$ [Fig. 2(b)], the degeneracy of the valleys is lifted but the electron-hole symmetry is still preserved. By increasing R, the magnetic confinement becomes important, as the energy levels approach the Landau levels (LLs) of an unbiased ABC-stacked TLG sheet, for which the states form a set of degenerate levels. The LLs of an ABC-stacked TLG sheet can be obtained from Refs. [50,51]. The well depth does not affect the higher energies since they are localized in the asymptotic region where the potential is constant. Consequently, these states behave as ABC-stacked TLG LLs. Due to the interplay between magnetic and electrostatic confinements, the spectrum shows level crossings which occur when the lower-energy states evolve into magnetically confined states with larger Landau indices by increasing the dot radius. These crossings occur for all states with $m \leqslant 0$ which contribute to the zero-energy LL. As a result of coupling between the gap- and magnetic-field-induced states, *anticrossings* of energy levels occur. We will consider this property in more detail in Sec. III B, ABA stacking.

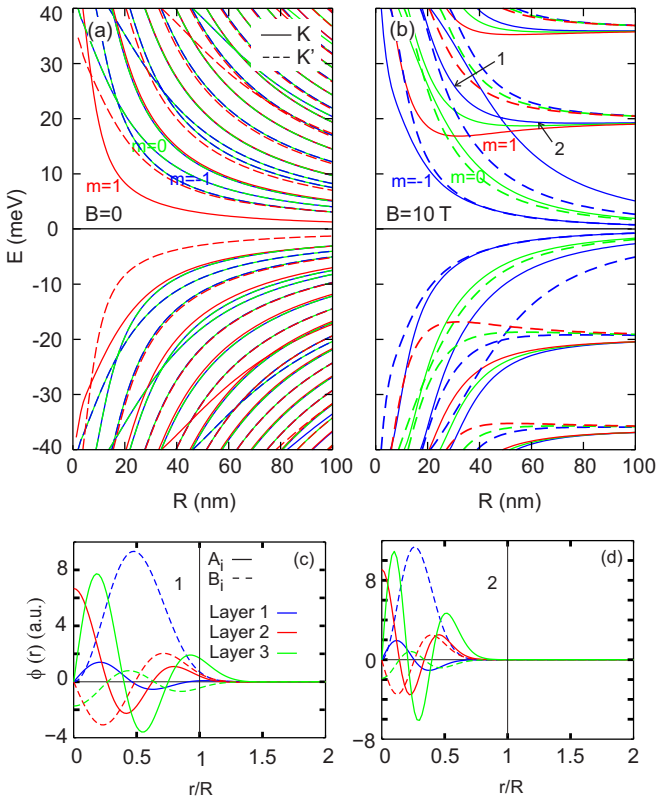

FIG. 2. (Upper panels) Lowest-energy states of an ABC-stacked TLG QD as a function of the dot radius R, for $m = -1$ (blue), $m = 0$ (green), and $m = 1$ (red), at the valleys K (solid) and K' (dashed) with (a) $B = 0$ and (b) $B = 10$ T. The well depth is $U_0 = 50$ meV. The spectrum for $B = 0$ is twofold degenerate due to the symmetry $E_K(m) = E_{K'}[-(m+1)]$. Both spectra also show the symmetry $E^e_K(m) = -E^h_{K'}(m)$. Lower panels (c) and (d) are the amplitude of the wave functions corresponding to, respectively, the points labeled by 1 and 2 in the energy spectrum of Fig. 2(b). Layer 1 (2, 3) is represented by the blue (red, green) curves. Sublattices A_i, (B_i) are represented by solid (dashed) curves.

The wave functions corresponding to the states labeled by 1 and 2 in the spectrum of Fig. 2(b) are shown in Figs. 2(c) and 2(d), respectively. As seen in Fig. 2(c), state 1 shows that the carrier is mostly confined in the dot region with decaying tail in the barrier region. On the other hand, state 2 [Fig. 2(d)], with the shallower wider potential, is completely confined inside the dot region indicating that magnetically confinement dominates. It is worth mentioning that the amplitudes of the spinor component corresponding to $B1$ and $A3$ sublattices are largest and more spread out over the dot. The $A2$ sublattice spinor component is the only one which is centered around $r = 0$ with nonzero value at $r = 0$.

As a function of the well depth U_0, the energy spectrum is shown in Figs. 3(a) and 3(b) in the absence ($B = 0$) and presence ($B = 10$ T) of magnetic field, respectively. The results are shown for $m = -2$ (black), $m = -1$ (blue), $m = 0$ (green), $m = 1$ (red), and $m = 2$ (purple) at the valleys K (solid curves) and K' (dashed curves) with dot radius $R = 25$ nm. For $B = 0$, beyond the energies $E = \pm U_0$ [delimited by the black dashed lines in Fig. 3(a)] the spectrum is continuous (yellow regions) and the bound states appear in the band gap ($\sim 2U_0$). Increasing the well depth removes the degeneracy of the lowest-energy states, as seen by realizing the more discreet energy levels in the band gap. Due to the Mexican-hat shape of the low energies in a biased ABC stacking TLG [see Fig. 1(a)], the exact value of the band gap is smaller than $2U_0$. This is the reason for the extension of the continuous spectrum to the right of the $E = \pm U_0$ lines, as seen in Fig. 3(a). When the field B is present, the continuous spectrum is absent [see Fig. 3(b)]. For $U_0 \to 0$ the results are the LLs of an unbiased ABC-stacked TLG QD, which are degenerate for different m as well as valleys. Further increase of

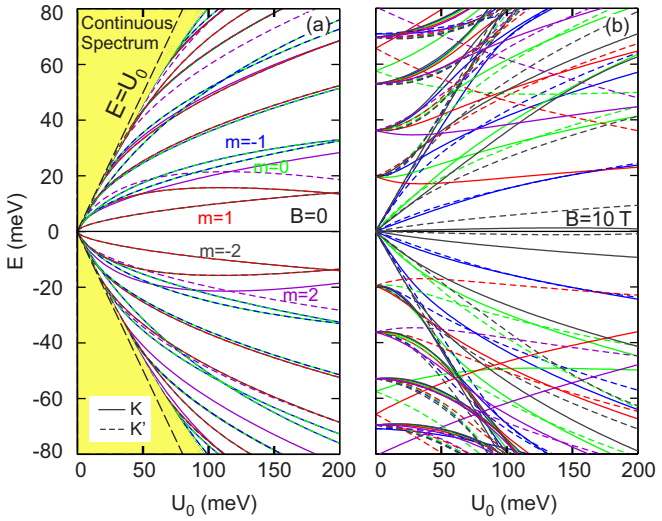

FIG. 3. Energy levels of an ABC-stacked TLG QD as a function of the well depth U_0 for $m = -2$ (black), $m = -1$ (blue), $m = 0$ (green), $m = 1$ (red), and $m = 2$ (purple) at the valleys K (solid) and K' (dashed) with (a) $B = 0$ and (b) $B = 10$ T. The dot radius is $R = 25$ nm. Due to the symmetry of $E_K(m) = E_{K'}[-(m+1)]$ the spectrum for $B = 0$ is twofold degenerate and both spectra show the symmetry $E^e_K(m) = -E^h_{K'}(m)$. The yellow region in (a) indicates the continuous spectrum for $B = 0$.

the well depth U_0 breaks this degeneracy and the spectrum becomes strongly dependent on m.

In Fig. 4(a), we show the energy levels as a function of the magnetic field B, at the K valley, for angular momenta $m = -2$ (black), $m = -1$ (blue), $m = 0$ (green), $m = 1$ (red), and $m = 2$ (purple) with $U_0 = 50$ meV and dot radius $R = 25$ nm. For the two angular momenta, $m = -1$ and 0, the spectrum is plotted at both valleys K and K' in Fig. 4(b). For $B = 0$ bound states exist in the symmetric band gap $2U_0$ and are degenerate because of the equality $E_K(m) = E_{K'}[-(m+1)]$ [see Fig. 4(a)]. For $B \neq 0$, this degeneracy is lifted, especially that of the lowest states, but electron-hole symmetry $E^e_K(m) = -E^h_{K'}(m)$ is still preserved. For large fields, magnetic confinement becomes important. If confinement is absent, the energy levels merge into the LLs (black dotted curves) of a pristine ABC-stacked TLG sheet. As is evident from Fig. 4(a), the lowest electron energy level corresponding to $m = -2$ crosses the zero-energy level at about $B \sim 11$ T, and approaches the zero LL as a hole state. In general, this holds for the $m < -2$ levels as well. Similar to the previous study of ABC-stacked TLG QD with infinite-mass boundary condition [39], the states with $m \leqslant 0$ in both valleys form the zero-energy LL in the conduction and valence bands.

B. ABA stacking

Figure 5 shows the lowest-energy levels of an ABA-stacked TLG QD, as a function of the dot radius R, for $m = -1$ (blue curves), $m = 0$ (green curves), and $m = 1$ (red curves), $U_0 = 50$ meV, at the two valleys K (solid) and K' (dashed), with (a) $B = 0$ and (b) $B = 10$ T. For $B = 0$, bound states appear in the energy gap ($\Delta_g = U_0/2$) beyond which the spectrum is continuous (yellow regions). Moreover, the

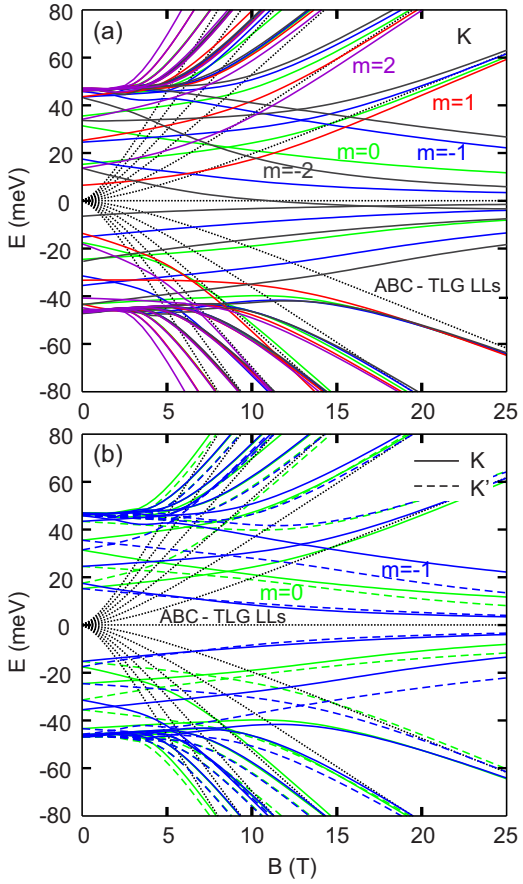

FIG. 4. (a) The lowest-energy levels of an ABC-stacked TLG QD as a function of the magnetic field B, with $U_0 = 50$ meV and dot radius $R = 25$ nm for the K valley. The angular momenta are $m = -2$ (black), $m = -1$ (blue), $m = 0$ (green), $m = 1$ (red), and $m = 2$ (purple). The dotted curves show the Landau levels of an unbiased ABC-stacked TLG. (b) As in (a) for $m = -1$ and $m = 0$ at the two valleys K and K'.

spectrum is twofold degenerate due to the symmetry $E_K(m) = E_{K'}[-(m-1)]$. A set of energy levels exists near $E = 0$ at small radii as a result of the Mexican-hat-shaped low-energy dispersion in a biased ABA-stacked TLG [see Fig. 1(d)]. Further, the lowest electron energy level $E(m = 1)$ of the ABA-stacked TLG dot is smaller than that of the ABC-stacked one when $B = 0$ (cf. Fig. 9). In presence of the magnetic field, as shown in Fig. 5(b), the mentioned degeneracy between the valleys K and K' is broken and the energy levels approach the LLs of ABA-stacked TLG [see Eqs. (6) and (7) in Ref. [50]]. Similar to the ABC-stacked case, here too the spectrum shows level crossings due to the interplay between magnetic and electrostatic confinements. These crossings occur for all states with $m \leqslant 0$ which contribute to the zero-energy LL. Also here, coupling between the gap- and magnetic-field-induced states can result in the formation of anticrossings in the energy spectrum. For example, as shown in the inset of Fig. 5(b), anticrossings appear in the shown energy range when the magnetic field is low, e.g., $B = 1$ T. A strong magnetic field can suppress the couplings reducing the size of the anticrossings.

Results for the spectrum of an ABA-stacked TLG QD, of radius $R = 25$ nm, as a function of the well depth U_0

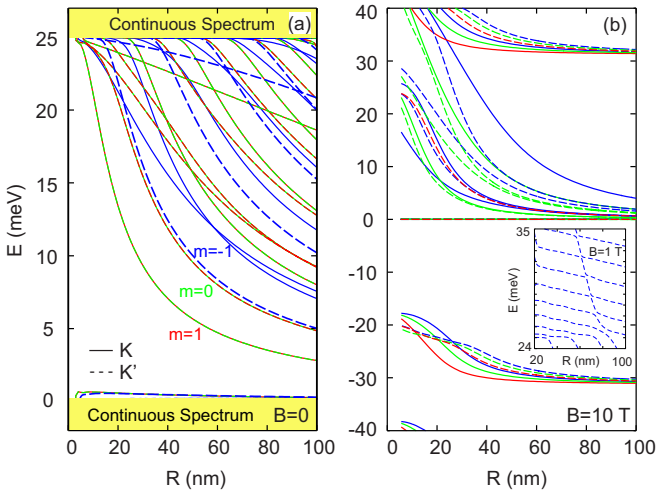

FIG. 5. Energy levels of ABA-stacking TLG QD as a function of dot radius R, for the angular momenta $m = -1$ (blue), $m = 0$ (green), and $m = 1$ (red), with $U_0 = 50$ meV at the two valleys K (solid) and K' (dashed) when (a) $B = 0$ and (b) $B = 10$ T. For $B = 0$, the spectrum is twofold degenerate due to the symmetry $E_K(m) = E_{K'}[-(m-1)]$. The inset shows examples of anticrossings due to the hybridization between the gap- and magnetic-field-induced states at low magnetic fields, e.g., $B = 1$ T, for $m = -1$ at the K' valley.

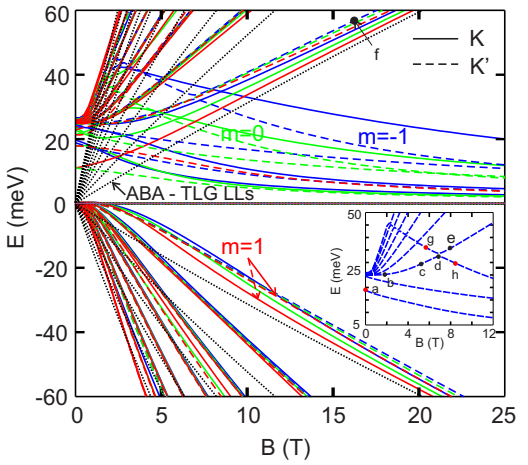

FIG. 7. Energy spectrum of an ABA-stacked TLG QD as a function of the magnetic field B, with $U_0 = 50$ meV and dot radius $R = 25$ nm at the K (solid curve) and K' (dashed curve) valleys. The blue, green, and red curves are for angular momenta $m = -1$, 0, and 1, respectively. The black dotted curves show the Landau levels of an ABA-stacked TLG sheet. The inset shows an enlarged view of the spectrum, showing the anticrossings for angular momentum $m = -1$ and the K' valley.

are shown in Fig. 6. The angular momenta are $m = -1$ (blue), $m = 0$ (green), $m = 1$ (red). The solid and dashed curves are for the K and K' valleys, respectively, in both zero magnetic field (a) and $B = 10$ T (b). For $B = 0$ and $U_0 = 0$, the spectrum is continuous (yellow regions) while a finite U_0 induces an asymmetric band gap $\sim U_0/2$. The value of the band gap starts to deviate from the value of $U_0/2$ with increasing U_0, as delimited by the black dashed lines in Fig. 6(a). This deviation can be linked to the Mexican-hat-shaped low-energy dispersion for a biased ABA-stacked

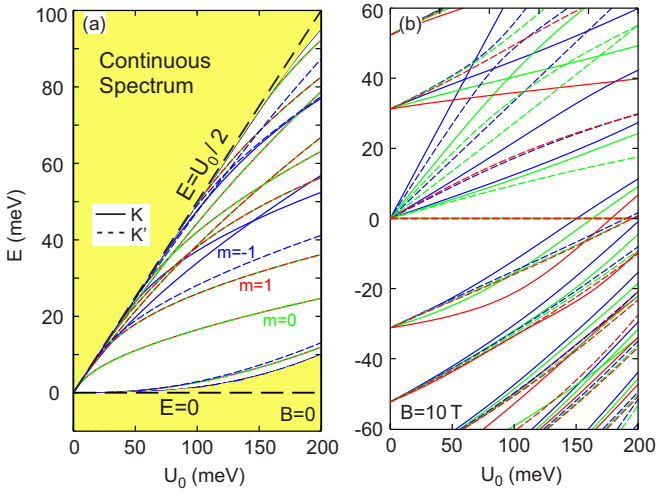

FIG. 6. Energy spectrum of an ABA-stacked TLG QD, of radius $R = 25$ nm, as a function of the well depth U_0 for $m = -1$ (blue), $m = 0$ (green), and $m = 1$ (red), at the valleys K (solid) and K' (dashed), with (a) $B = 0$ and (b) $B = 10$ T. The yellow region in (a) shows the continuous $B = 0$ spectrum.

TLG which is more pronounced for large gate potentials. The formation of discrete levels (which reflect the confined states) depends on the angular momentum and the well depth. As seen in Fig. 6(a), large $|m|$ requires a large potential to realize confined states. Due to the opening of an asymmetric energy gap, unlike in the ABC-stacked case, the hole bound states are absent at zero magnetic field. The magnetic field removes the degeneracy of the continuous spectrum and makes the energy levels discreet as shown in Fig. 6(b). For $U_0 = 0$, we have the LLs of an unbiased ABA-stacked TLG sheet, being degenerate for different m's and valleys, as expected. However, as the well depth increases, the electrostatic confinement becomes important, as seen by the removal of their $U_0 = 0$ degeneracies. Further, as seen in Fig. 6(b), the electron states are more affected than the hole ones for $B \neq 0$. In other words, increasing U_0 weakens the confinement of the negative energy states as seen by the lower resolution of the discrete levels at these energies. The same behavior is seen for the gap-induced MLG QDs in a quantum well potential [4].

The lowest-energy levels of an ABA-stacking TLG QD, as a function of the field B, are shown in Fig. 7 for $m = -1$ (blue), $m = 0$ (green), and $m = 1$ (red) at the valleys K (solid curve) and K' (dashed curve). Here, the well depth is $U_0 = 50$ meV and dot radius $R = 25$ nm. For $B = 0$, bound states appear in the asymmetric energy gap ($\sim U_0/2$) in the positive range of energy. Notice the difference with ABC stacking in which the gap $2U_0$ is symmetric (see Fig. 4), and bound states exist above and below $E = 0$. Increasing the field B, the degeneracy of the m levels as well as that of the valleys are lifted due to the breaking of time-reversal symmetry. At high magnetic fields, the energy levels merge into the LLs (black dotted curves) of an unbiased ABA-stacking TLG sheet. The gap-induced states can *hybridize* with states induced by the magnetic field resulting in the formation of anticrossings for energy levels

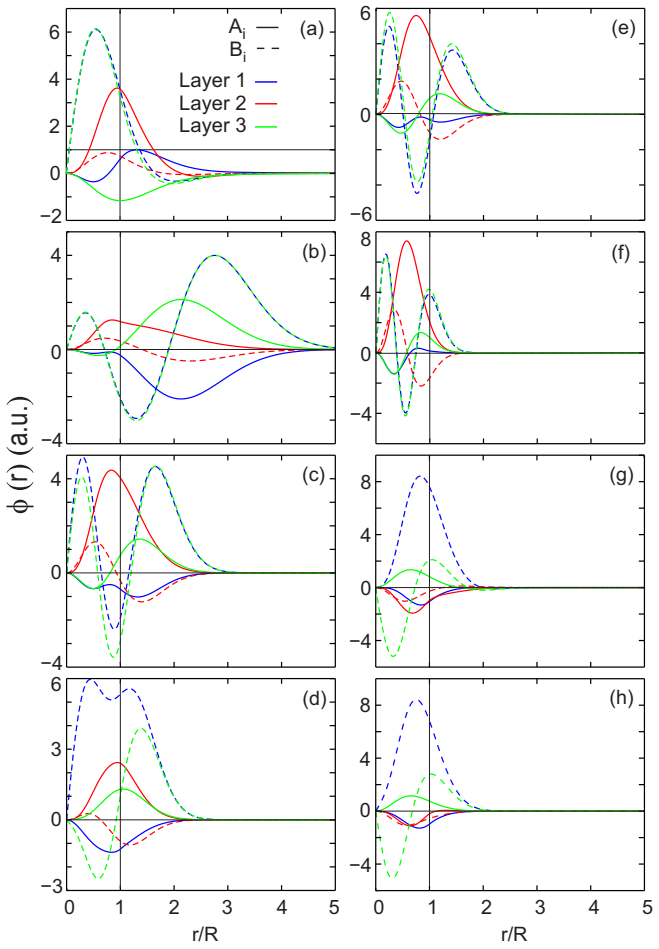

FIG. 8. The wave functions corresponding to the energies marked by (a)–(h) in Fig. 7. Layer 1 (2, 3) is represented by the blue (red, green) curves. Sublattices A_i (B_i) are represented by solid (dashed) curves.

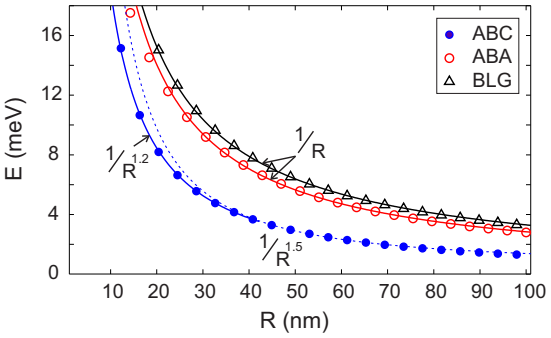

FIG. 9. Lowest-electron-energy levels ($m = 1$ at the K valley) for an ABC-, ABA-stacked TLG QD, and for a AB-stacked BLG QD (blue filled, red open circles, and black open triangles, respectively). The fitting (solid curves) shows a $\sim a/R$ dependence for the ABA-stacked TLG and AB-stacked BLG dots. For the ABC-stacked TLG dot, the fitting shows a $\sim a/R^{1.2}$ (blue solid curve) and $\sim a/R^{1.5}$ (blue dashed curve) dependence at small and large radii, respectively. The well depth is $U_0 = 50$ meV and the corresponding fitting parameter a, in units of meV $\times$ nm, is equal to 283.7 (ABA), 279.9 (BLG), 280.2 (ABC, $R \lesssim 40$ nm), and 854.6 (ABC, $R \gtrsim 40$ nm).

belonging to the same m (see inset of Fig. 7). The spectrum shows crossings between energy levels with different m and valleys. In contrast with the ABC-stacked dot, only electron states contribute to the zero-energy LL.

To demonstrate the way of hybridization of the gap- and magnetic-field-induced states, we plot, in Fig. 8, the spinor components for the energies labeled by (a)–(h) in the inset of Fig. 7. As a result of the gap, for $B = 0$ only one bound state appears in it with energy $E_a \approx 18.86$ meV. The corresponding quantum state is shown in Fig. 8(a). As seen, the carrier is mostly confined inside the dot region, but still the spinors have a substantial amplitude in the barrier region. The presence of the carrier in the barrier region is a result of Klein tunneling. As B increases, the magnetic-field-induced states couple to the upper continuum energies merging into the unbiased ABA-stacked TLG LLs via anticrossings. Before and away from the anticrossing point [e.g., Fig. 8(b)], the coupling is weak and the state has a large amplitude in the barrier region. Near and right at the anticrossing [e.g., Figs. 8(c), 8(d), 8(e), 8(g), and 8(h)], the coupling is strong and, hence, the amplitude of each state inside the dot region is large. Then, as B increases, the amplitude of spinors in the barrier is gradually suppressed and the state becomes confined near the center of the dot. This occurs, for example, for Fig. 8(f). Comparison of the states Figs. 8(a), 8(g), and 8(h), marked by red circles, with Figs. 8(b)–8(f) (black circles) shows that the latter ones typically have extra nodes. As seen in the most of the states, the behavior of the spinors at the $B1$ and $B3$ sublattices are similar to each other. This is expected as we can see from the ABA-stacked TLG structure in Fig. 1(b), in which the $B1$ and $B3$ sublattices physically have the same status except for the applied potentials. On the other hand, the spinors of $B1$, $B3$, and $A2$ atoms possess large amplitudes. They can be occupied at low energies which do not have a counterpart atom in the other layers.

In Fig. 9, we compare the results of the lowest-electron-energy levels ($m = 1$ for the K valley), versus dot radius, for three types of QDs, i.e., ABC-, ABA-stacked TLG and AB-stacked BLG with $U_0 = 50$ meV [for BLG we set $U_1 = -U_2 = U_b(r)$]. They are marked by blue filled, red open circles, and black open triangles, respectively. The solid curves show the fittings to the power-law dependence $\approx R^\alpha$. The ground-state energies of the ABA-stacked TLG and AB-stacked BLG dots exhibit a $\sim 1/R$ dependence. This can be understood by recalling that the width of the electron state l_0 in a 2D electron gas system with a parabolic potential $V(\mathbf{r}) = \omega_0^2 r^2/2$ is proportional to $1/\sqrt{\omega_0}$. In analogy with this, we note that the ABA TLG and AB BLG sheets have a quadratic low-energy dispersion $E \sim k^2 \sim 1/l_0^2 = \omega_0$. In our case, the parabolic potential profile $U(r) = (U/R^2)r^2$ gives $\omega_0 \propto 1/R$ and consequently the lowest-energy level $E_{\min} \propto 1/R$. In a similar manner, considering the cubic low-energy dispersion of an ABC TLG sheet, one has $E \sim k^3 \sim 1/l_0^3 \sim \omega_0^{3/2}$ which results in $E \propto 1/R^{1.5}$. Our fitting for the ABC-stacked TLG shows a $\sim 1/R^{1.2}$ dependence for $R \lesssim 40$ nm and $\sim 1/R^{1.5}$ for $R \gtrsim 40$ nm. The different α value at small radii is due to the Mexican-hat-shaped (i.e., noncubic dispersion) low-energy spectrum which is relevant for small dot sizes. For ABC-stacked TLG and AB-stacked BLG QDs, resulting from

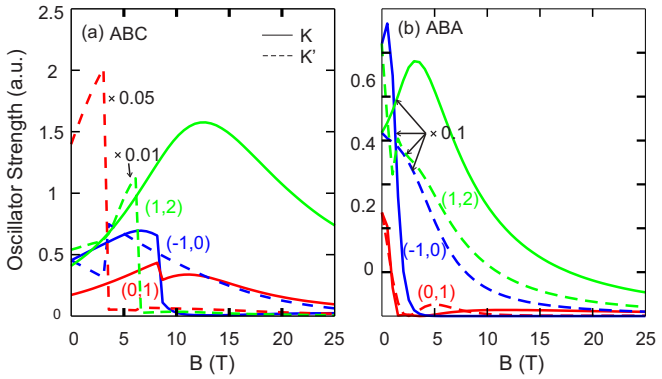

FIG. 10. Oscillator strengths for the dipole-allowed transitions $(-1,0)$ (blue), $(1,0)$ (red), and $(1,2)$ (green) as a function of magnetic field B, in (a) ABC- and (b) ABA-stacked TLG QD. The solid and dashed curves pertain to the K and K' valleys, respectively.

an infinite-mass boundary condition, the lowest-energy levels show a $\sim 1/R^3$ [39] and $\sim 1/R^2$ [52] dependence. This can be linked to the fact that, unlike for parabolic confinement, the wave-function width for an infinite-mass potential is analogous to that for hard-wall confinement and given by the size of the dot.

C. Oscillator strength

Finally, we evaluate the oscillator strengths for both stackings using Eqs. (12) and (13). The dipole-allowed transitions $(m,m') \equiv (-1,0)$ (blue), $(0,1)$ (red), and $(1,2)$ (green), which correspond to the transitions between the lowest-energy levels, are shown as functions of the magnetic field B in Fig. 10 for (a) an ABC stacking and (b) an ABA stacking. The solid curves are for the K valley and the dashed ones for the K' valley. As shown, there is a significant difference between the results of the two stackings. For the ABC stacking, the results show that the dipole-allowed transitions (1,2) and (0,1) at the K' valley are predominant at low magnetic fields but they decay with increasing B and other transitions become stronger. For the ABA stacking, except for small B fields ($B \lesssim 1.2$ T) in which the transition $(-1,0)$ from the K valley is remarkable, for other magnetic fields the predominant transition is (1,2) from the K valley. Due to the crossings of the energy levels in Figs. 4 and 7, sudden changes occur in the transitions at these points. As can be seen, all transitions decay by increasing the magnetic field. At large B ($B \gtrsim 15$ T), all transitions are suppressed due to the strong localization of the states at the center of the dot, resulting in vanishing overlap between the wave functions. This B-field dependence of the oscillator strengths is strikingly different from that of the corresponding oscillator strengths in extended graphene sheets [53], which do not show such a reduction with B, and results from an entirely different QD spectrum and reduced overlap of the eigenfunctions involved.

IV. SUMMARY AND CONCLUDING REMARKS

We studied the energy levels of electrostatically confined quantum dots in TLG and investigated their dependence on a perpendicular magnetic field B, and contrasted the results of the two most stable layer stackings, the ABC and ABA stackings. Our numerical results for parabolic confining potentials are expected to approximate well those of the actual potentials. Similar to gate-defined QDs in BLG [23,24], the TLG QDs we studied can be realized experimentally by, e.g., the application of nanostructured gates.

We showed that the energy spectra exhibit the intervalley symmetry $E^e_K(m) = -E^h_{K'}(m)$ for electron (e) and hole (h) states, where m is the angular momentum quantum number and K,K' the two valleys. For $B = 0$ the electron and hole spectra are twofold degenerate due to the symmetry $E_K(m) = E_{K'}[-(m+1)]$. A Mexican-hat-shaped gap exists in the spectrum for finite potential on the bottom layer $U_0 \neq 0$ of either stacking but as U_0 increases so does the continuous spectrum albeit slightly. For finite B, bound states are created in this gap and the $B = 0$ degeneracies are lifted. The lowest-energy levels show a $\sim 1/R$ dependence on the dot radius R, for ABA-stacked TLG. For the ABC-stacked TLG, the lowest electron state exhibits a $\sim 1/R^{1.2}$ dependence at small radii and $\sim 1/R^{1.5}$ at large radii. This is in contrast with the $1/R^3$ one for ABC-stacked dots created by an infinite-mass boundary condition.

As functions of the magnetic field, the corresponding oscillator strengths for the dipole-allowed transitions differ drastically between the two stackings. For either stacking, they also differ drastically from those of unconfined TLG [53] especially at strong magnetic fields.

The present calculations are for single-particle states. For many particle QDs, one has to include the Coulomb interaction which may importantly affect the energy spectrum as was shown recently for a BLG QD (two electrons) in Ref. [54].

Note added. Recently, we came across numerical simulations of a gate-defined ABC-stacked TLG QD [55]. In this work, however, a less realistic step electrostatic potential was used.

ACKNOWLEDGMENTS

This work was supported by the Flemish Science Foundation (FWO-Vl) and the Methusalem foundation of the Flemish Government (F.M.P., M.M.), the University Research Fund (BOF) (M.Z.), and the Canadian NSERC Grant No. OGP0121756 (P.V.).

[1] M. I. Katsnelson, K. S. Novoselov, and A. K. Geim, Nat. Phys. **2**, 620 (2006).
[2] A. Matulis and F. M. Peeters, Phys. Rev. B **77**, 115423 (2008).
[3] H.-Y. Chen, V. Apalkov, and T. Chakraborty, Phys. Rev. Lett. **98**, 186803 (2007).
[4] G. Giavaras and F. Nori, Phys. Rev. B **83**, 165427 (2011).
[5] G. Giovannetti, P. A. Khomyakov, G. Brocks, P. J. Kelly, and J. van den Brink, Phys. Rev. B **76**, 073103 (2007).

[6] B. Sachs, T. O. Wehling, M. I. Katsnelson, and A. I. Lichtenstein, Phys. Rev. B **84**, 195414 (2011).

[7] S. Y. Jung, G. M. Rutter, N. N. Klimov, D. B. Newell, I. Calizo, A. R. H. Walker, N. B. Zhitenev, and J. A. Stroscio, Nat. Phys. **7**, 245 (2011).

[8] A. Luican-Mayer, M. Kharitonov, G. Li, C.-P. Lu, I. Skachko, Alem-Mar B. Goncalves, K. Watanabe, T. Taniguchi, and E. Y. Andrei, Phys. Rev. Lett. **112**, 036804 (2014).

[9] E. Tovari, P. Makk, P. Rickhaus, C. Schönenberger, and S. Csonka, Nanoscale **8**, 11480 (2016).

[10] P. Rickhaus, M.-H. Liu, P. Makk, R. Maurand, S. Hess, S. Zihlmann, M. Weiss, K. Richter, and C. Schönenberger, Nano Lett. **15**, 5819 (2015).

[11] G. Giavaras, P. A. Maksym, and M. J. Roy, J. Phys.: Condens. Matter **21**, 102201 (2009).

[12] G. Giavaras and F. Nori, Phys. Rev. B **85**, 165446 (2012).

[13] S. Moriyama, Y. Morita, E. Watanabe, and D. Tsuya, Appl. Phys. Lett. **104**, 053108 (2014).

[14] N. M. Freitag, L. A. Chizhova, P. Nemes-Incze, C. R. Woods, R. V. Gorbachev, Y. Cao, A. K. Geim, K. S. Novoselov, J. Burgdörfer, F. Libisch, and M. Morgenstern, Nano Lett. **16**, 5798 (2016).

[15] A. D. Güçlü, P. Potasz, M. Korkusinski, P. Hawrylak, X. Li, S. P. Lau, L. Tang, R. Ji, and P. Yang, *Graphene Quantum Dots* (Springer, Berlin, 2014).

[16] Z. Z. Zhang, K. Chang, and F. M. Peeters, Phys. Rev. B **77**, 235411 (2008).

[17] M. Zarenia, A. Chaves, G. A. Farias, and F. M. Peeters, Phys. Rev. B **84**, 245403 (2011).

[18] A. V. Rozhkov, G. Giavaras, Y. P. Bliokh, V. Freilikher, and F. Nori, Phys. Rep. **503**, 77 (2011).

[19] P. Recher and B. Trauzettel, Nanotechnology **21**, 302001 (2010).

[20] E. McCann, D. S. L. Abergel, and V. I. Falko, Solid State Commun. **143**, 110 (2007).

[21] J. M. Pereira Jr., P. Vasilopoulos, and F. M. Peeters, Nano Lett. **7**, 946 (2007).

[22] J. M. Pereira Jr., F. M. Peeters, P. Vasilopoulos, R. N. Costa Filho, and G. A. Farias, Phys. Rev. B **79**, 195403 (2009).

[23] T. Allen, J. Martin, and A. Yacoby, Nat. Commun. **3**, 934 (2012).

[24] A. M. Goossens, S. C. M. Driessen, T. A. Baart, K. Watanabe, T. Taniguchi, and L. M. K. Vandersypen, Nano Lett. **12**, 4656 (2012).

[25] M. S. Dresselhaus and G. Dresselhaus, Adv. Phys. **51**, 1 (2002).

[26] M. Koshino and E. McCann, Phys. Rev. B **87**, 045420 (2013).

[27] Y. Zhang, J. P. Small, W. V. Pontius, and Ph. Kim, Appl. Phys. Lett. **86**, 073104 (2005).

[28] A. C. Ferrari, J. C. Meyer, V. Scardaci, C. Casiraghi, M. Lazzeri, F. Mauri, S. Piscanec, D. Jiang, K. S. Novoselov, S. Roth, and A. K. Geim, Phys. Rev. Lett. **97**, 187401 (2006).

[29] C. Berger, Z. Song, T. Li, X. Li, A. Y. Ogbazghi, R. Feng, Z. Dai, A. N. Marchenkov, E. H. Conrad, P. N. First, and W. A. de Heer, J. Phys. Chem. B **108**, 19912 (2004).

[30] C. J. Shih, A. Vijayaraghavan, R. Krishnan, R. Sharma, J. H. Han, M. H. Ham, Z. Jin, S. Lin, G. L. C. Paulus, N. F. Reuel, Q. H. Wang, D. Blankschtein, and M. S. Strano, Nat. Nanotechnol. **6**, 439 (2011).

[31] P. Mahanandia, F. Simon, G. Heinrich, and K. K. Nanda, Chem. Commun. **50**, 4613 (2014).

[32] M. F. Craciun, S. Russo, M. Yamamoto, J. B. Oostinga, A. F. Morpurgo, and S. Tarucha, Nat. Nanotechnol. **4**, 383 (2009).

[33] K. F. Mak, J. Shan, and T. F. Heinz, Phys. Rev. Lett. **104**, 176404 (2010).

[34] W. Bao, L. Jing, J. Velasco, Jr, Y. Lee, G. Liu, D. Tran, B. Standley, M. Aykol, S. B. Cronin, D. Smirnov, M. Koshino, E. McCann, M. Bockrath, and C. N. Lau, Nat. Phys. **7**, 948 (2011).

[35] C. H. Lui, Z. Li, K. F. Mak, E. Cappelluti, and T. F. Heinz, Nat. Phys. **7**, 944 (2011).

[36] K. Zou, F. Zhang, C. Clapp, A. H. MacDonald, and J. Zhu, Nano Lett. **13**, 369 (2013).

[37] T. Khodkov, I. Khrapach, M. F. Craciun, and S. Russo, Nano Lett. **15**, 4429 (2015).

[38] A. A. Avetisyan, B. Partoens, and F. M. Peeters, Phys. Rev. B **81**, 115432 (2010).

[39] M. Mirzakhani, M. Zarenia, D. R. da Costa, S. A. Ketabi, and F. M. Peeters, Phys. Rev. B **94**, 165423 (2016).

[40] F. Guinea, A. H. Castro Neto, and N. M. R. Peres, Phys. Rev. B **73**, 245426 (2006).

[41] F. Zhang, B. Sahu, H. Min, and A. H. MacDonald, Phys. Rev. B **82**, 035409 (2010).

[42] E. McCann, *Electronic Properties of Monolayer and Bilayer Graphene*, Graphene Nanoelectronics (Springer, Berlin, 2011), p. 237.

[43] B. Partoens and F. M. Peeters, Phys. Rev. B **74**, 075404 (2006).

[44] R. Quhe, J. Ma, Z. Zeng, K. Tang, J. Zheng, Y. Wang, Z. Ni, L. Wang, Z. Gao, J. Shi, and J. Lu, Sci. Rep. **3**, 1794 (2013).

[45] Y.-P. Wang, X.-G. Li, J. N. Fry, and H.-P. Cheng, Phys. Rev. B **94**, 165428 (2016).

[46] M. Koshino and E. McCann, Phys. Rev. B **79**, 125443 (2009).

[47] For more details, see the COMSOL MULTIPHYSICS website: http://www.comsol.com

[48] J. M. Pereira Jr., F. M. Peeters, and P. Vasilopoulos, Phys. Rev. B **76**, 115419 (2007).

[49] S. M. Reimann and M. Manninen, Rev. Mod. Phys. **74**, 1283 (2002).

[50] Sh. Yuan, R. Roldán, and M. I. Katsnelson, Phys. Rev. B **84**, 125455 (2011).

[51] S. H. R. Sena, J. M. Pereira Jr., F. M. Peeters, and G. A. Farias, Phys. Rev. B **84**, 205448 (2011).

[52] D. R. da Costa, M. Zarenia, A. Chaves, G. A. Farias, and F. M. Peeters, Carbon **78**, 392 (2014).

[53] S. H. R. Sena, J. M. Pereira Jr., G. A. Farias, and F. M. Peeters, Phys. Rev. B **86**, 085412 (2012).

[54] M. Zarenia, B. Partoens, T. Chakraborty, and F. M. Peeters, Phys. Rev. B **88**, 245432 (2013).

[55] H. Xiong, W. Jiang, Y. Song, and L. Duan, J. Phys.: Condens. Matter (2017), doi: 10.1088/1361-648X/aa6aac.